nks
Nordisk kernesikkerhedsforskning
Norrænar kjarnöryggisrannsóknir
Pohjoismainen ydinturvallisuustutkimus
Nordisk kjernesikkerhetsforskning
Nordisk kärnsäkerhetsforskning
Nordic nuclear safety research

NKS-246
ISBN 978-87-7893-318-8

In-vessel Coolability and Steam Explosion in Nordic BWRs

Weimin Ma, Liangxing Li, Roberta Hansson, Walter Villanueva,
Pavel Kudinov, Louis Manickam, Chi-Thanh Tran

Royal Institute of Technology (KTH), Sweden

May 2011

Abstract

The objective of this research is to reduce the uncertainty in quantification of steam explosion risk and in-vessel coolability in the Nordic BWR plants which employ cavity flooding as severe accident management (SAM) strategy.

To quantify the coolability of debris bed packed with irregular particles, the friction laws of fluid flow in particulate beds packed with non-spherical particles were investigated on the POMECO-FL test facility, and the experimental data suggest that the Ergun equation is applicable if the effective particle diameter of the particles is represented by the equivalent diameter of the particles, which is the product of Sauter mean diameter and shape factor of the particles. One-way coupling analysis between PECM model for melt pool heat transfer and ANSYS thermo-structural mechanics was performed to analyze the vessel creep, and the results revealed two different modes of vessel failure: a ‘ballooning’ of the vessel bottom and a ‘localized creep’ concentrated within the vicinity of the top surface of the melt pool. Single-droplet steam explosion experiments were carried out by using oxidic mixture of WO_3-CaO, and the results show an apparent difference in steam explosion energetics between the eutectic and non-eutectic melts at low melt superheat (100 ^{o}C).

Key words

severe accident, debris coolability, steam explosion

NKS-246
ISBN 978-87-7893-318-8

Electronic report, May 2011

NKS Secretariat
P.O. Box 49
DK - 4000 Roskilde, Denmark

Phone +45 4677 4045
Fax +45 4677 4046
www.nks.org
e-mail nks@nks.org

Contract AFT/NKS-R(10)75/4

Research Report

In-vessel Coolability and Steam Explosion in Nordic BWRs

Weimin Ma, Liangxing Li, Roberta Hansson, Walter Villanueva, Pavel Kudinov, Louis Manickam, Chi-Thanh Tran

Division of Nuclear Power Safety
Department of Physics
Royal Institute of Technology (KTH)

May 2010

Executive Summary

The objective of the project "In-vessel Coolability and Steam Explosion in Nordic BWRs", dubbed INCOSE, is to reduce the uncertainty in quantification of steam explosion risk and in-vessel coolability in the Nordic BWR plants with the cavity flooding as a severe accident management (SAM) measure.

During 2010 substantial advances and new insights into physical mechanisms were gained for: (i) the friction laws of particulate beds packed with irregular particles, which are of important to coolability analysis of debris beds; (ii) the creep of the lower head of a BWR under thermo-mechanical loads; and (iii) the effect of binary oxides mixture's properties on steam explosion. For the friction laws of particulate beds packed with irregular particles, the POMECO-FL experimental data suggest that the Ergun equation is applicable if the effective particle diameter of the particles is represented by the equivalent diameter of the particles, which is the product of Sauter mean diameter and shape factor of the particles. For molten pool interaction with the vessel, one-way coupling between PECM model for melt pool heat transfer and ANSYS thermo-structural mechanics was employed to analyze the vessel creep, and the results revealed two different modes of vessel failure: a 'ballooning' of the vessel bottom and a 'localized creep' concentrated within the vicinity of the top surface of the melt pool. The preliminary results of steam explosion experiments performed at low melt superheat (100 ^{o}C) using oxidic mixture of WO_3-CaO detect an apparent difference in steam explosion energetics between the eutectic and non-eutectic materials.

Contents

1. Introduction

The goal of the severe accident research at Kungliga Tekniska Högskolan (KTH) is to create knowledge base for resolution of two long-standing severe accident issues, namely steam explosion and corium coolability in severe accident scenarios of Nordic BWRs which adopt cavity flooding as the cornerstone of Severe Accident Management (SAM) measures.

For this objective, the resecrh project INCOSE (In-vessel Coolability and Steam Explosion in Nordic BWRs) is focused on two areas of highest return: (i) in-vessel coolability with svere accident management (SAM) action (e.g., CRGT cooling), and (ii) steam explosion energetics in case of vessel failure, which may threaten the containment itegrity.

The relationship between the two research topics are as shown in Fig. 1, directed by a risk oriented approach. The research focus is to identify the weakest links in the picture and to reduce uncertainties in quantification of (i) in-vessel corium coolability which provides the limiting boundary conditions (reactor vessel failure mode and timing, corium ejection characteristics – composition, total mass and release rate) for steam explosion in the ex-vessel scenarios, and (ii) micro interactions of steam explosion which provide limiting mechanisms for steam explosion energetics.

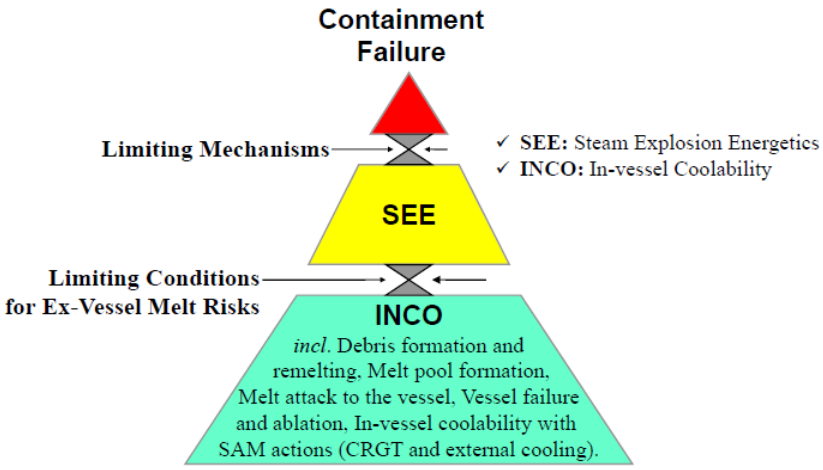

Fig. 1: Risk-oriented approach in identification of the research topics.

This report summarizes the progress and achievements of the project during Year 2010. The resesrch activity has a synergic collaboration with Swedish APRI-7 research program, EU SARNET2 Excellence Network for severe accident research and OECD SERENA-II project dedicated to understaning of steam explosion in reactor safety.

2. Results and Discussions

2.1. In-vessel coolability

The in-vessel coolability study at KTH is focused on *a*) quantification of the effectiveness of control rod guide tubes (CRGT) cooling as a potential severe accident management (SAM) measure in BWRs; *b*) reduction of the uncertainty in coolability analysis of a debris bed formed in the RPV during a postulated severe accident. The in-vessel coolability study

is of critical importance for reduction of uncertainty in the ex-vessel phenomena, since it does not assess the possibility of in-vessel melt retention but also provides melt release conditions if the vessel fails, such as failure mode (single/multiple jets), size of the breach, amount of melt which can be ejected at vessel failure, melt composition, melt superheat. One important element in the in-vessel coolability study is to consider potential severe accident management measures (e.g., CRGT cooling, external vessel cooling) to bounding uncertainties in phenomena.

2.1.1. Coolability of in-vessel debris bed

The research on this topic is concerned with reducing the uncertainty in coolability analysis of a debris bed which may be formed from fuel coolant interactions (FCIs) in the reactor pressure vessel (RPV) during various stages (cf. Fig. 2a & 2b) of a severe accident scenario. Due to its internal pores which facilitate coolant ingress, the debris bed provides more chances to remove the decay heat than a molten corium pool where coolant access is very limited (only to surface). Thus, debris bed coolability plays an important role in the termination and stabilization of a severe accident.

To analyze the experiments and finally assess debris coolability in reactor application, a great number of analytical models [1-6] and empirical correlations were developed for prediction of two-phase flow (friction) and heat transfer (dryout heat flux) in packed beds. The central point in modeling was to provide the formulation of the friction laws for momentum equations of single and two-phase flow in porous media.

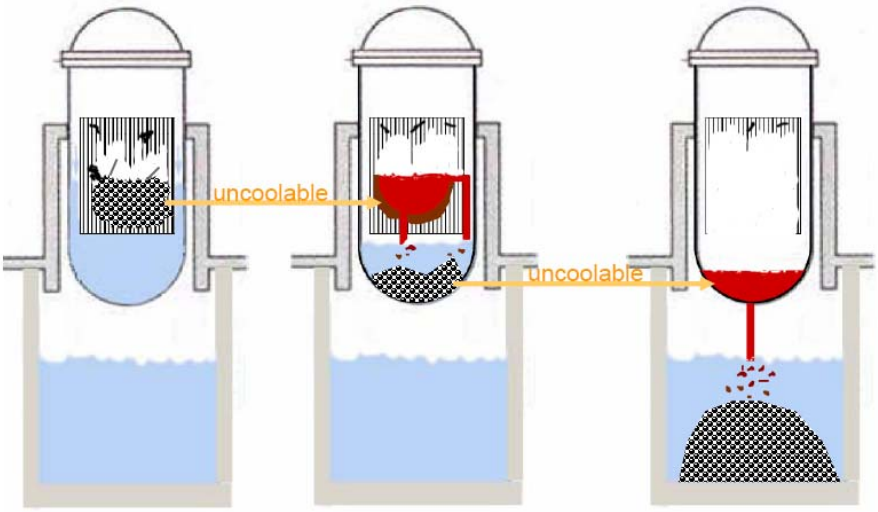

(a) in the core ***(b)*** in the lower plenum ***(c)*** in the reactor cavity

Fig. 2: Debris bed formation during different stages of a severe accident scenario.

The momentum equation of single-phase flow through porous media can be expressed by the Ergun equation [7]:

$$-\frac{dp}{dz} = \frac{\mu}{K} J + \frac{\rho}{\eta} J^2 \qquad (1)$$

where dp/dz is the pressure gradient along the bed, ε is the porosity, μ is the dynamic viscosity of fluid, d is the diameter of particles, ρ is the density of the fluid and J is the

superficial velocity of fluid. For uniform spherical particles bed, the permeability K and passability η are taken as

$$K = \frac{\varepsilon^3 d^2}{150(1-\varepsilon)^2} \qquad \eta = \frac{\varepsilon^3 d}{1.75(1-\varepsilon)} \tag{2}$$

where, d and ε are particle diameter and porosity of the debris bed, respectively.

Ergun's equation was adapted to two-phase flow in porous media by the inclusion of relative permeability, relative passability and interfacial friction:

$$-\frac{dp_l}{dz} = \rho_l g + \frac{\mu_l}{K \cdot K_{r,l}} J_l + \frac{\rho_l}{\eta \cdot \eta_{r,l}} J_l \cdot |J_l| - \frac{F_i}{1-\alpha} \tag{3}$$

$$-\frac{dp_g}{dz} = \rho_g g + \frac{\mu_g}{K \cdot K_{r,g}} J_l + \frac{\rho_g}{\eta \cdot \eta_{r,g}} J_g \cdot |J_g| + \frac{F_i}{\alpha} \tag{4}$$

where J_l and J_g are the superficial velocities of fluids; and K_r and η_r are relative permeability and relative passability that differ from model to model as listed in Table 1, where the interfacial friction F_i is also defined.

Table 1. Relative permeability and passability in models for coolability analysis.

Parameter / **Model**	K_r	η_r	F_i
Lipinski (1981) [3]	$K_{r,l}= s^3$ $K_{r,g}=\alpha^3$	$\eta_{r,l}=s^3$ $\eta_{r,g}=\alpha^3$	0
Reed (1982) [4]	$K_{r,l}= s^3$ $K_{r,g}=\alpha^3$	$\eta_{r,l}= s^5$ $\eta_{r,g}=\alpha^5$	0
Hu & Theofanous (1991) [5]	$K_{r,l}= s^3$ $K_{r,g}=\alpha^3$	$\eta_{r,l}= s^6$ $\eta_{r,g}=\alpha^6$	0
Schulenberg & Műller (1987) [6]	$K_{r,l}= s^3$ $K_{r,g}=\alpha^3$	$\eta_{r,l}= s^5$ $\eta_{r,g}=\alpha^6$, α>0.3 $\eta_{r,g}=0.1\alpha^4$, α≤0.3	$F_i = 350 s^7 \alpha \frac{\rho_l K}{\eta\sigma}(\rho_l - \rho_g) g \left(\frac{J_g}{\alpha} - \frac{J_l}{s}\right)^2$

From the above equations, one can see the particle diameter is an important parameter to determine flow friction (and therefore dryout heat flux) of a porous bed. Nevertheless, the identification of particle diameter is not straightforward when the bed is composed of multi-size and/or irregular particles, as in the case for rector application where the debris particles are non-spherical and having a wide range of size distribution.

For the mixture of particles with a size distribution, the mean particle diameter is very different even for the same combination of multi-size spheres, depending on which size distribution function (mass, area, length, number, etc.) to be chosen [8]. Accordingly, there exist among others the mass mean diameter, area mean diameter, length mean diameter and number mean diameter. Which one is suitable for coolability analysis of a debris bed? For a particulate bed packed with multi-diameter particles, our previous study [9] shows that at low flowrate (Re<7) the effective particle diameter used in the Ergun equation can be represented by the area mean diameter of the particles in the bed, while at high velocity (Re>7) the effective particle diameter is closer to the length mean diameter. If the area mean

diameter (Sauter mean diameter) is chosen as the effective particle diameter in the models as shown in Table 1, the frictional pressure drop of two-phase flow in the bed can be predicted by the Reed model with a good agreement.

For a particulate bed packed with non-spherical particles (e.g., cylinders, hollow spheres, hollow cylinders, or rings), some research works in this aspect showed that much higher pressure drops have been obtained than anticipated from the calculations based on spheres [10-12]. The increase in tortuosity was considered as the reason why non-spherical particle beds generated higher pressure drop.

For prediction of frictional pressure drop in the bed packed with non-spherical particles, a generally-accepted approach by most researchers is to introduce a shape factor (sphericity) in the Ergun equation, which is defined as the ratio of the surface area of equivalent-volume sphere to that of the actual particle [13]:

$$\psi = \frac{surface\ \ of\ \ sphere\ \ of\ equal\ \ volume\ \ to\ \ the\ \ particle}{surface\ \ area\ \ of\ \ the\ \ particle} = \frac{\pi^{\frac{1}{3}}\left(6V_p\right)^{\frac{2}{3}}}{A_p} \tag{5}$$

where V_p is volume of the particle, A_p the surface area of the particle.

In the present study, experiment is performed to reveal that the Ergun equation is capable of predicting the pressure drop of fluid flow in the packed beds with the non-spherical particles, if the effective particle diameter is equal to the product of Sauter mean diameter and the shape factor:

$$d_{eq} = \psi d_{sd} \tag{6}$$

which is called the equivalent particle diameter here.

Test facility and test beds

The experiment is carried out on the POMECO-FL test facility, as illustrated in Fig. 3, which is basically an adiabatic water/air single- and two-phase flow loop for porous media. Major components of the test facility are made of transparent Plexiglas to facilitate visual observation. The test section accommodating the particles is made of a Plexiglas pipe with the inside diameter of 90mm and the height of 635mm. Four annular chambers for pressure tapping are designed to surround the pipe at different levels, with radial holes (0.5mm in diameter) uniformly distributed as opening from the bed to the annular chambers. The chambers do not only provide an average pressure reading over the entire circumference of each tapping point, but also prevent gas and particles from entering the impulse lines of pressure transducers. At both the inlet and the outlet of the test section, two pieces of stainless steel wire mesh are applied between the flanges to support the bed from below and prevent the particles from leaving the bed. Air is supplied from the bottom and flows up through the packed bed, but water can be supplied from either the bottom or the top for a bottom-fed (co-current flow) or a top-flooding (counter-current flow) bed.

Two Rosement-3051 differential pressure transmitters with high accuracy are mounted on the test section to measure entire and half pressures drops, respectively, of single or two-phase flow through the bed. Valve manifolds are used with the differential pressure transmitters to perform the block, equalizing and vent requirements of the transmitters. The

flowrates of gas and water flows are measured by seven OMEGA flowmeters with different measuring ranges. The pressure and temperature are monitored by using OMEGA pressure transducers and K-type thermocouples. The flowmeters and pressure transducers are calibrated prior to experiment.

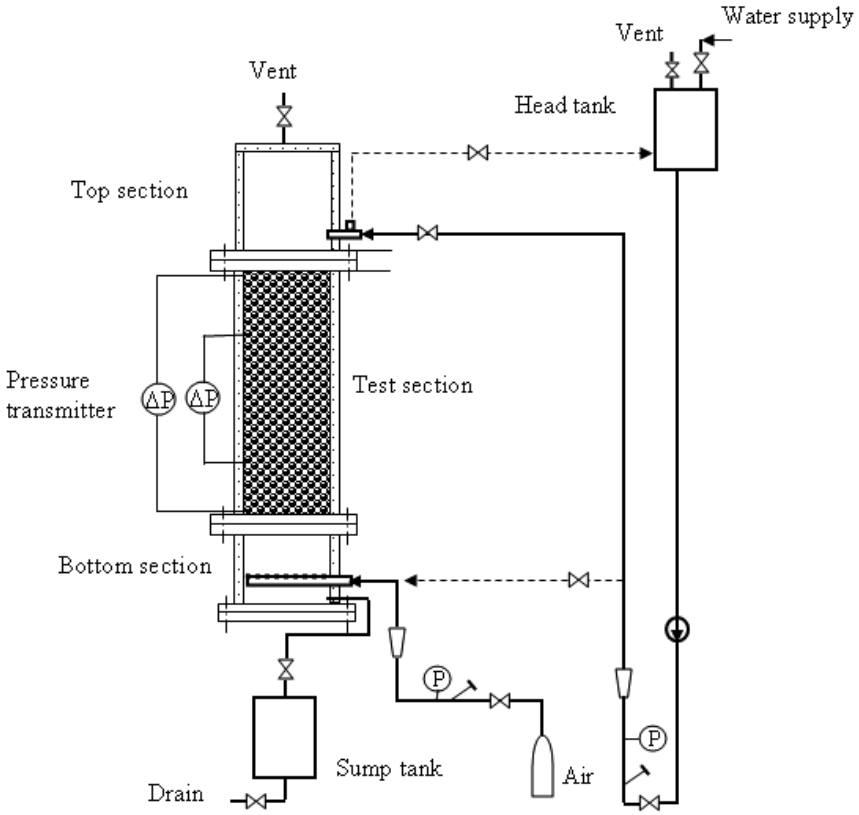

***Fig. 3*:** Schematic diagram of POMECO-FL facility

Since the prediction model is sensitive to the bed porosity as well as the particle size, yielding great difference in the prediction of pressure drop with a relatively small change in the two parameters, a great care is taken here in determining the bed porosity. This is achieved by accurate measurement of the material density (double check and verification of factory data) and the particle mass (free of moisture) loaded into the bed. The particles are well mixed prior to filling in the test section so that a uniform packed bed can be obtained.

Table 2. Test beds.

Bed	**Particles**	**diameter** *(mm)*	**hole** *(mm)*	**length** *(mm)*	ε *(/)*	d_{sd} *(mm)*	ψ *(/)*	d_{eq} *(mm)*
1	hollow spheres	6	1	/	0.39	5	0.845	4.2
2	hollow spheres	6	3	/	0.55	3	0.577	1.7
3	cylinders	3	/	3	0.337	3	0.874	2.6
4	cylinders	3	/	6	0.37	3.6	0.832	3

Table 2 lists the packed beds investigated in present study, while Fig. 4 shows the particles used in present study. The beds are all 635mm tall and 90mm in diameter. The particles used in the particulate beds (Bed-1 through Bed-4) are hollow spheres and cylinders. The hollow spheres have holes made through the solid balls concentrically.

(a) (b) (c) (d)

Fig. 4: Particles used in the present study

(a) glass hollow spheres 6×1 mm (ball diameter × hole diameter); (b) stainless steel hollow spheres 6×3 mm; (c) stainless steel cylinder 3×3 mm (diameter × length); (d) stainless steel cylinder 3×6 mm.

After the well mixed particles are uniformly loaded into the test section, the fluid (air or water for single phase flow) is supplied to flow through the packed bed at low velocity until there is no change in bed height and in flow resistance, to make sure that the fluid floods the bed and has access to all the pores. For the measurement of pressure drop, the impulse lines of the differential pressure transmitters are filled with single phase fluid by proper operation of the valve manifolds, so that the effect of gravity on pressure drop reading can be excluded. Prior to any measurements taken, the facility is running for no less than half an hour to establish steady-state conditions throughout the system. After the steady-state data are recorded by the data acquisition system, adjust the operational parameters (say, the flowrates) to other values, and repeat the same procedure.

In addition to the calibration of instrumentation, the test facility and its measurement system are qualified by measurements of single-phase flow through particulate bed packed with single-size glass spheres of diameter 1.5mm/3mm/6mm. The porosity is 0.37 for the bed. The measured pressure gradients are compared with those predicted by the Ergun equation, and the quality of experimentation and instrumentation is ensured by good agreements [9].

Results and discussion

Figure 5 shows the pressure gradients of water flow through Bed-1 packed by hollow glass spheres with individual diameter of 6 mm and centric hole of 1 mm. The experimental data (triangle symbols) are underestimated if the Sauter mean diameter d_{sd} was taken as the effective particle diameter. However, the measured pressure drops were well predicted by Eq. (1) in case of $d=d_{eq}$, as shown in Fig. 5. This implies that in this case the effective particle diameter can be represented by the equivalent diameter of the particles, as defined in Eq. (2), the product of Sauter mean diameter and the shape factor. Such characteristics hold for Bed-2 packed by hollow spheres with individual diameter of 6 mm and centric hole of 3 mm; see Fig. 6.

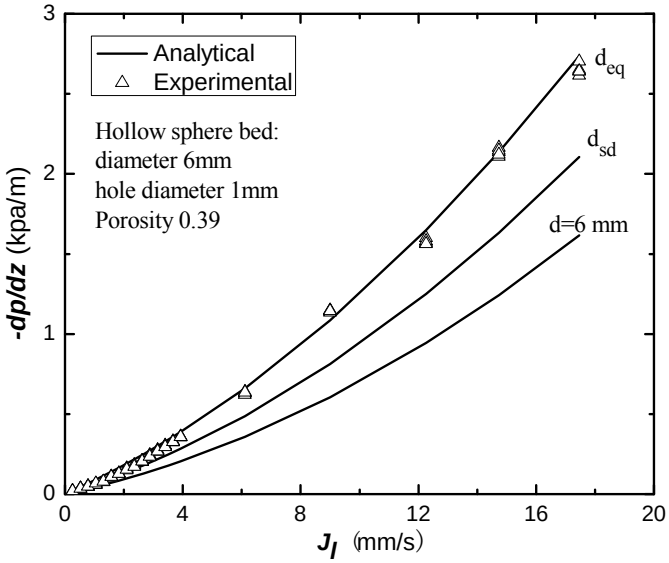

***Fig. 5*:** Pressure gradient of water flow in Bed-1 packed by hollow spheres (6-mm-diameter spheres with 1-mm-centric holes; porosity of the bed=0.39).

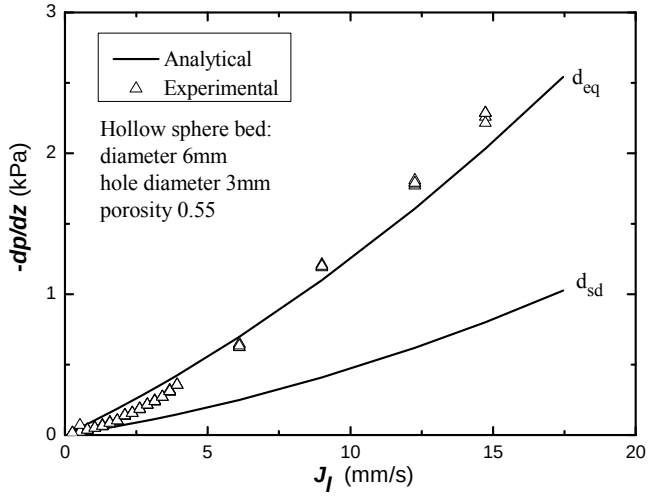

Fig. 6: Pressure gradient of water flow in Bed-2 packed by hollow spheres (6-mm-diameter spheres with 3-mm-centric holes; porosity of the bed=0.555)

Table 3 shows the key parameters for Bed-1 and Bed-2, both packed with hollow spheres. For Bed-1, the Sauter mean diameter is 5 mm and the equivalent diameter 4.2mm that is equal to the effective particle diameter d_e=4.2 mm derived from experimental data through Eq. (1). The equivalent diameter of the particles in Bed-2 is 1.7 mm that is not equal, but close to the effective particle diameter d_e =1.8mm. The deviation may be due to the much smaller shape factor (0.577) and higher porosity (0.555) of Bed-2. Nevertheless, compared with the Sauter mean diameter (3 mm) of the bed, the equivalent diameter is still much more comparable to the effective particle diameter, and deviation of the prediction can be considered within uncertainty margin. It is therefore concluded that the pressure drops of fluid flow through the hollow-spherical-particle beds can be predicted by the Ergun equation if the effective particle diameters are represented by the equivalent diameters of the particles in the beds.

Table 3. Data of Bed-1 and Bed-2 packed with hollow spheres.

Bed	Particles	diameter *(mm)*	hole *(mm)*	ε *(/)*	d_{sd} *(mm)*	ψ *(/)*	d_{eq} *(mm)*	d_e *(mm)*
1	hollow spheres	6	1	0.39	5	0.845	4.2	4.2
2	hollow spheres	6	3	0.555	3	0.577	1.7	1.8

Generally speaking, Eq. (1) using Sauter mean diameters also underestimates the pressure drops of fluid flow through Bed-3 and Bed-4 packed with cylindrical particles, but its predictions using equivalent particle diameters have good agreements with the experimental data; see Figs. 7 and 8. Bed-3 is packed with 3-mm-diameter and 3-mm-long cylinders, while Bed-4 is packed with 3-mm-diameter and 6-mm-long cylinders. The porosity is 0.34 and 0.37 for Bed-3 and Bed-4, respectively. It seems that at low flowrate (J_l < 7 mm/s) the pressure gradients are better predicted by using Sauter mean diameter. This means the shape factor plays a less significant role at laminar flow regime and only the specific surface area (reflected in the Sauter mean diameter) can cover the influence of particle morphology on flow drag in the beds. When the fluid velocity is high, turbulence prevails and the specific surface area alone is no longer sufficient to count the contribution of particle morphology to the pressure drops. The impact of shape factor should be more explicit and pronounced. In applications, turbulent flow regime is more common, and thus the predictions by the equivalent particle diameter should be more conservative

Table 4 shows the key parameters for Bed-3 and Bed-4 within the flowrate range performed in the experiments. For Bed-3, the Sauter mean diameter d_{sd}=3 mm, the equivalent diameter d_{eq}=2.6 mm and the effective particle diameter d_e=2.6 mm. For Bed-4, d_{sd} =3.6 mm, d_{eq}=3 mm and d_e=3 mm. One can see that within the whole flowrate range, the effective mean particle diameters are equal to the equivalent diameters rather than the Sauter mean diameters of the particles in the beds. As the conclusion for hollow-spherical-particle beds, the pressure drops of fluid flow through the cylindrical-particle beds can be predicted by the Ergun equation if the equivalent diameters of the particles in the beds are chosen.

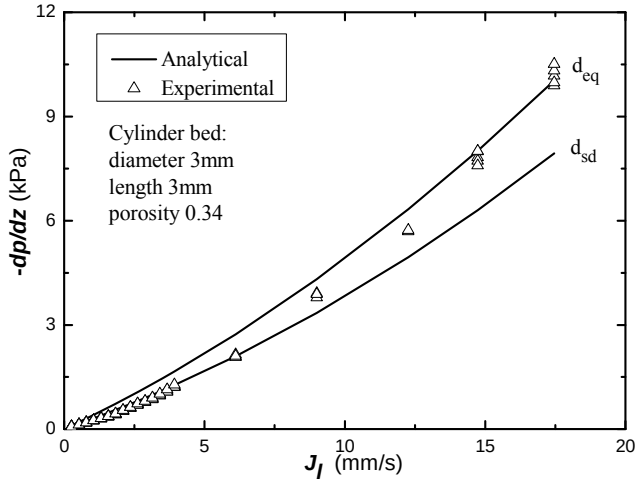

Fig. 7: Pressure gradient of water flow in Bed-3 packed by cylindrical particles (3-mm-long 3-mm-diameter cylinders; porosity of the bed=0.34).

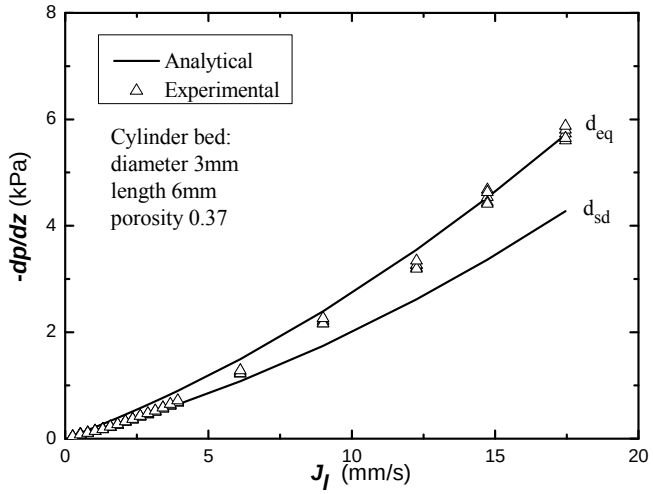

Fig. 8: Pressure gradient of water flow in Bed-4 packed by cylindrical particles (6-mm-long 3-mm-diameter cylinders; porosity of the bed=0.37).

Table 4. Data of Bed-3 and Bed-4 packed with cylindrical particles.

Bed	**Particles**	**diameter** *(mm)*	**length** *(mm)*	ε *(/)*	d_{sd} *(mm)*	ψ *(/)*	d_{eq} *(mm)*	d_e *(mm)*
3	cylinders	3	3	0.34	3	0.874	2.6	2.6
4	cylinders	3	6	0.37	3.6	0.832	3	3

2.1.2. Vessel creep under melt attack with CRGT cooling

To perform a mechanistic multi-dimensional analysis of heat transfer in the corium-filled lower head, further development and validation of Effective Convective Model (ECM) and Phase-change Effective Convective Model (PECM) were developed at KTH [15], which incorporate the advantages of the modern CFD method and the available correlation-based method, being able to simulate melt pool behavior in a complex geometry as the BWR's lower plenum with a forest of CRGTs. The focus of year 2010 is placed on performing analysis for vessel creep under thermal and mechanical loads [16].

A coupled thermo-mechanical creep analysis of the pressure vessel lower head was carried out to provide insights into failure modes of the reactor pressure vessel under the thermal load of melt pool with CRGT cooling. We consider two cases with different melt pool depths H = 0.7 m and 1.0 m. In each case we observe different modes of failure if only CRGT cooling is applied.

Fig. 9 shows the von Mises creep strains and displacements of the vessel wall for the case with melt pool depth H = 0.7 m. At time t = 5.14 h (Fig. 9c), the maximum creep strain has reached 0.19 located along the vicinity of the top of the melt pool while most part of the lower section has creep strains between 0.06-0.12. The maximum displacement becomes 0.34 m at the bottom center of the pressure vessel and gets smaller as reaching the top of the pool, which indicates a 'ballooning' type of deformation. The rest of the vessel has negligible displacement. This ballooning intensifies at a later time t = 5.56 h (Fig. 9c) and shall result in vessel failure, although we cannot consider the displacements and creep

strains at this time to be reliably predicted since the maximum creep strain (0.42) has reached beyond the validated range of the creep modeling. To demonstrate the importance of the creep to vessel failure, Fig. 9d shows a thermo-mechanical analysis with the same thermal load but without creep modeling in mechanical analysis at time t = 5.56 h and the maximum mechanical and thermal strain has only reached 0.009 with a maximum displacement of 0.05 m.

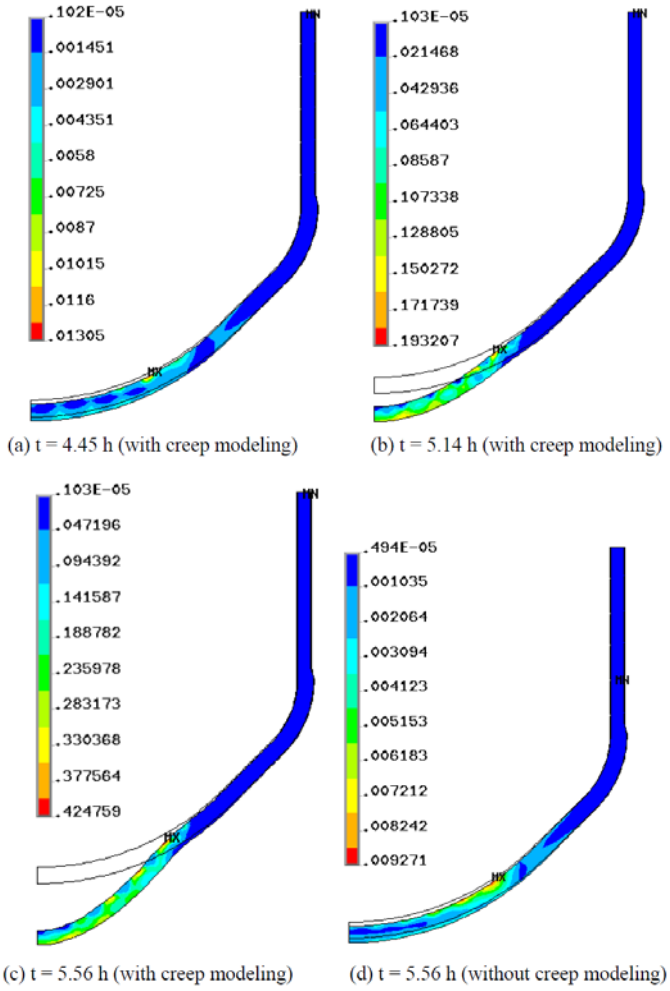

(a) t = 4.45 h (with creep modeling) (b) t = 5.14 h (with creep modeling)

(c) t = 5.56 h (with creep modeling) (d) t = 5.56 h (without creep modeling)

Fig. 9: von Mises creep strains and displacements at different times with melt pool depth of 0.7 m. The maximum displacements are (a) 0.04 m, (b) 0.34 m, (c) 0.72 m, and (d) 0.05 m.

In Fig. 10 the von Mises creep strains and displacements are shown for the case with melt pool depth H = 1 m. At time t = 3.89 h in Fig. 10a, the maximum creep strain has reached 0.01 located in the vicinity of the top of the melt pool while the maximum displacement is 0.03 m. It becomes clear in Fig. 10b that the strains are localized in the region right below the pool top surface. In addition, the displacement of the lower part of the vessel is almost uniform at 0.07 m. The observation suggests a different mode of failure which is, localized creep, as compared with the ballooning type in the previous case. Moreover, we can see the same qualitative behavior in Fig. 10c as the localized creep intensifies in the same location.

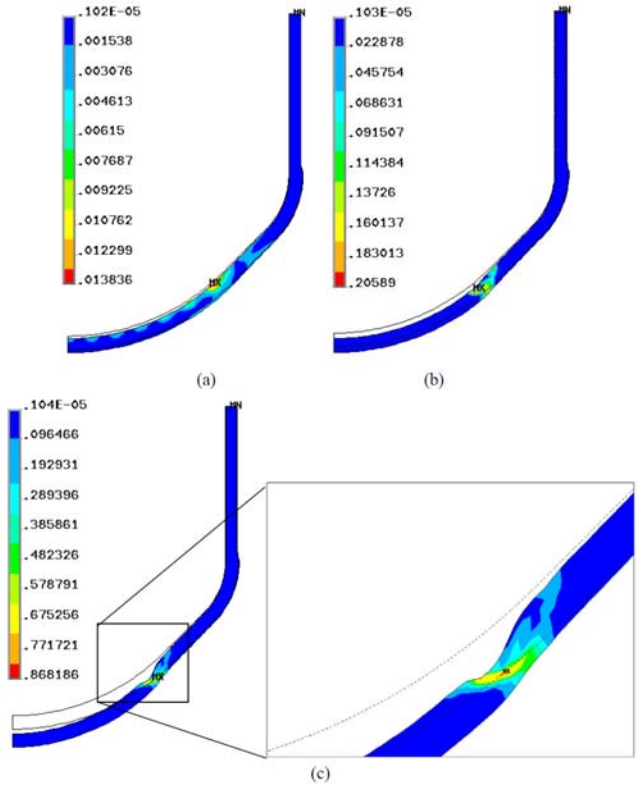

Fig. 10: von Mises creep strains and displacements with melt pool depth of 1 m at at (a) 3.89 h, (b) 4.49 h, and (c) 4.72 h. The maximum displacements are (a) 0.03 m, (b) 0.07 m, and (c) 0.25 m.

2.2. Steam explosion energetics

The objective of the steam explosion study at KTH is to pursue new evidences of corium low explosivity by performing MISTEE experiments. The new focus during 2010 is to perform MISTEE experiment with eutectic and non-eutectic single oxidic molten droplet.

After testing of different oxidic materials (e.g., MoO_3-Bi_2O_3, MnO-TiO_2, MoO_3-ZrO_2, MnO-MoO_3, MoO_3-TiO_2 and WO_3-Bi_2O_3), the binary mixture of WO_3-CaO (whose phase diagram is as shown in Fig. 9) was selected to perform single droplet steam explosion experiment.

The test facility named MISTEE (Micro Interactions in Steam Explosion Experiments) shown in Fig. 10 is designed for the visualization of the explosion of a single droplet disturbed by a weak pressure wave, characteristic of the early triggering phase in a vapor explosion. The facility consists of a test chamber, a melt generator, an external trigger system, an operational control system, and a data acquisition and visualization system.

The test section is a rectangular Plexiglas tank (180×130×250mm) in which a piezoelectric pressure transducer is flush-mounted at the center of the test section wall. A K-type thermocouple is employed to measure the water temperature inside the test section, and a C-type thermocouple is used to measure the molten droplet temperature in the furnace. The melt generator consists of an induction furnace (260V, 40A) and a graphite cylinder (40mm

O.D. × 50mm) with a molybdenum crucible (20mm I.D. × 30mm). A molten WO_3-CaO mass of ~1g is loaded to the crucible to guarantee the single-droplet delivery through a 5 mm hole at the center of the crucible bottom. The melt generator, which includes the induction coil and crucible, is housed inside a chamber into which argon gas is purged in to suppress the thermocouple oxidation and burning of the graphite crucible during the heating and melting phases. A tungsten plug is used to block the hole in the crucible bottom during the melting and this plug is lifted by a pneumatic piston to release the melt droplet. The external trigger system can be described as a piston located at the bottom of the test section, which generates the sharp pressure pulse (rising time of 50 μs at the full width half maximum) up to 0.15 MPa that travels through the coolant. The trigger hammer that impacts on the piston to generate a pressure pulse is aligned underneath the latter, and is driven by a rapid discharge of a capacitor bank, consisting of three capacitors of 400 Vdc and 4700 mF each.

The fast synchronous visualization system, SHARP (Simultaneous High-speed Acquisition of x-ray Radiography and Photography), consists of tungsten lighting and a high speed CMOS digital camera (Redlake HG50LE), up to 100000 fps (with 20000 fps rate used in the actual tests) for the photography; and a continuous X-ray source tube (Philips MCN 321 - max. 320 keV), an X-ray converter and an image intensifier coupled to a high speed camera (Lightning RDTPlus camera), for radiographic imaging up to 50000 fps (with 5000 fps rate used in the actual tests). Image processing methods were developed to process and synchronize the photographic and X-ray radiographic images acquired was developed [17]. A more detailed description of the equipment, test procedure, assessment of measurement uncertainty and image processing methods can be found elsewhere [18].

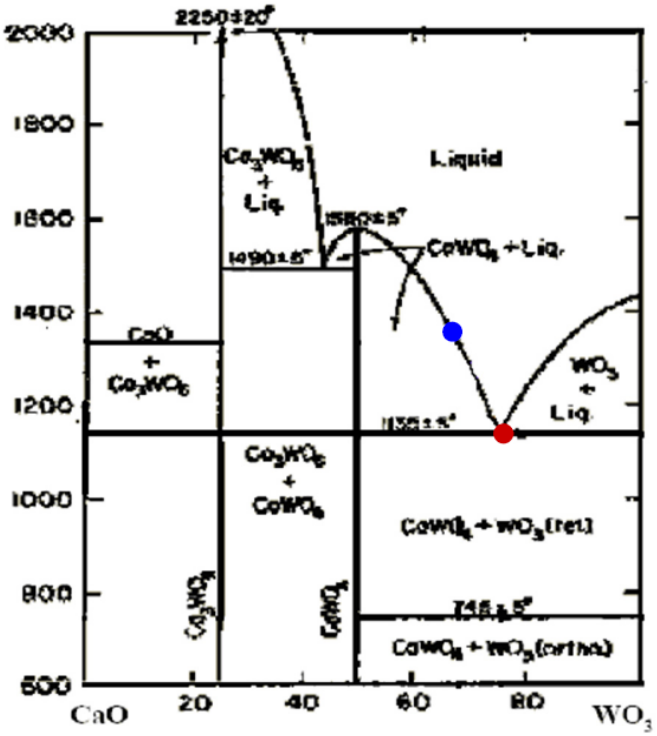

Fig. 9: Phase diagram of WO_3-CaO.

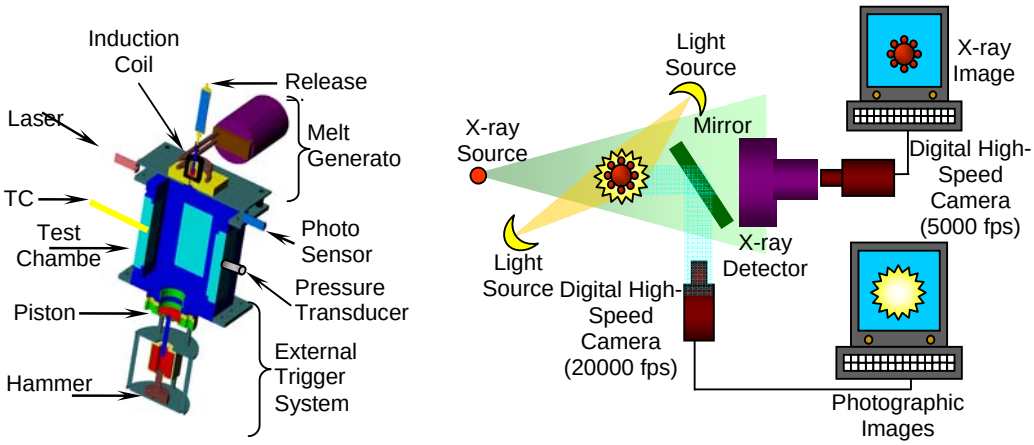

Fig. 10: MISTEE test section and SHARP visualization system.

Two series of externally triggered single-drop experiments, in which WO_3-CaO was used as the melt material and water as coolant, were performed on the MISTEE test facility. In the first test series, experiments with a eutectic composition (75:25 mol%, $T_{liquidus}$=1135°C,) and with a non-eutectic composition (72:27 mol%, $T_{liquidus}$=1232°C, $T_{solidus}$=1135°C, $\Delta T_{superheat}$~200°C) of WO_3-CaO, were performed under high subcooled coolant conditions (ΔT_{sub} ~80°C) and high initial melt superheat ($\Delta T_{superheat}$ ~200-300°C). In the second test series, similar water subcooling and melt compositions, i.e. eutectic and non-eutectic WO_3-CaO, were employed; the melt superheat, however, was lower (~100°C) than the first test series. From both series a number of tests were chosen for the actual analysis due to their data completeness, i.e. simultaneous record of bubble and melt dynamics. Still photographic images, with a temporal resolution of 0.05 ms per frame and the corresponding X-ray radiography images, with a temporal resolution of 0.2 ms per frame, are presented in Figures 11 to 14. The images reveal the vapor film and melt progression during the steam explosion of ~1 g of eutectic and non-eutectic molten WO_3-CaO droplet under high water subcooling, and different melt superheat. Similar to the single droplet experiments performed with a metallic melt (tin) [19], the vapor film dynamics produces three defined cycles of bubble expansion and collapse; see Fig 15. For convenience, we define t=0 ms at the final collapse of the first vapor bubble's cycle.

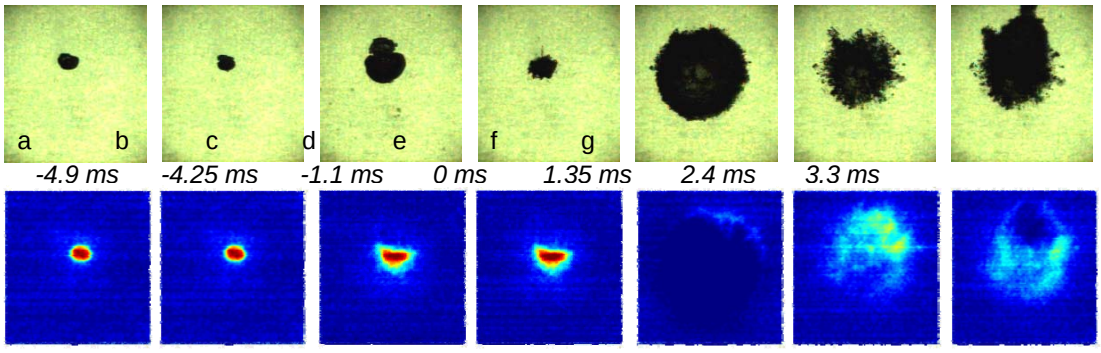

Fig. 11: Vapor film (top) and melt dynamics (bottom) of a single droplet of eutectic WO_3-CaO initially at 1350°C superheat, undergoing vapor explosion in water at 20°C.

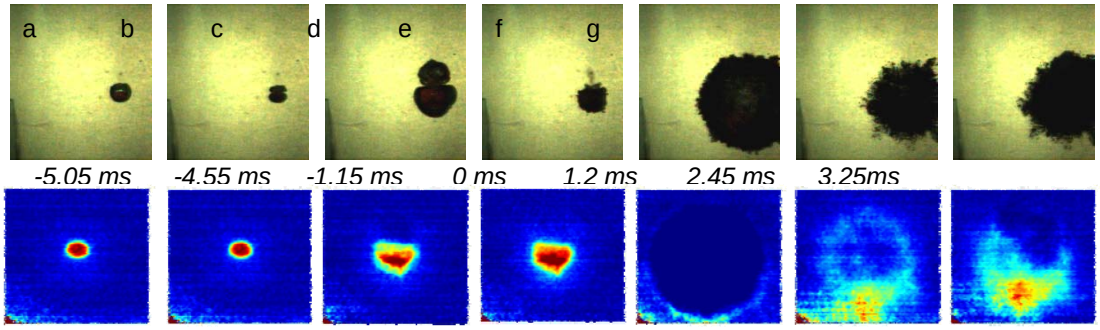

Fig. 12: Vapor film (top) and melt dynamics (bottom) of a single droplet of non-eutectic WO_3-CaO initially at 1480°C superheat, undergoing vapor explosion in water at 20°C.

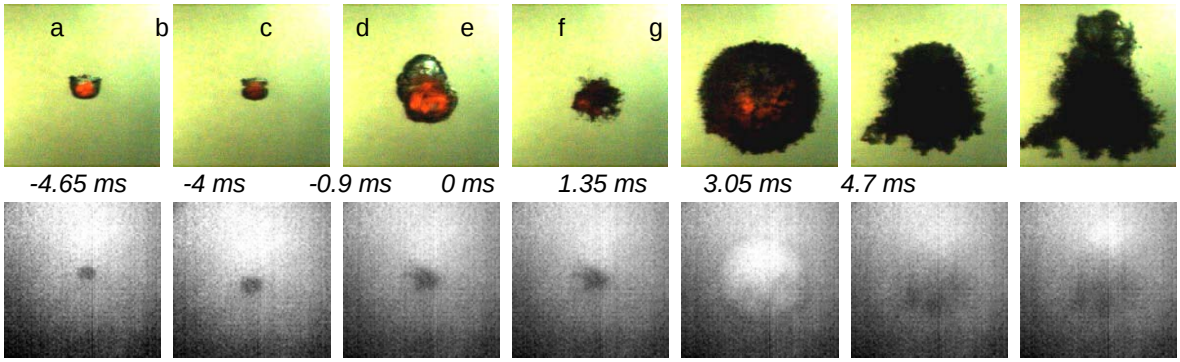

Fig. 13: Vapor film (top) and melt dynamics (bottom) of a single droplet of eutectic WO_3-CaO initially at 1251°C superheat, undergoing vapor explosion in water at 23°C.

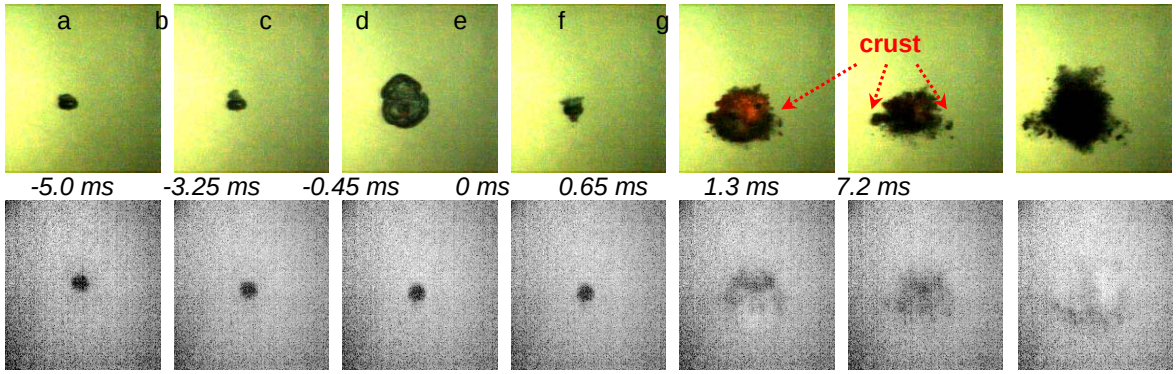

Fig. 14: Vapor film (top) and melt dynamics (bottom) of a single droplet of non-eutectic WO_3-CaO initially at 1350°C superheat, undergoing vapor explosion in water at 22°C.

Due to the melt's high temperature, a vapor film with a small dome on the rear side is immediately formed at the time the molten WO_3-CaO droplet enters the water, and endures as it descends into the water pool; Figs. 11a through 14a, with a velocity of ~0.47m/s. The interaction initiates when the external pressure wave destabilizes the vapor film (Figs. 11b through 14b), triggering the parallel oscillatory behavior of the bubble/ rear and cyclic jet formation underneath of the main bubble. Melt-coolant local contacts occur and subsequent nucleation takes place initiating the bubble's first cycle expansion. During this cycle, the vapor film dynamics creates complex internal flows that disturb the melt droplet surface

facilitating its deformation/pre-fragmentation, i.e. preconditioning. That can be clearly seen in the radiographic images, in which the initial elliptical droplet, Figs. 11-14a (bottom), evolves into a convoluted droplet with fine fragments present in the droplet's periphery, Figs. 11-14c (bottom). The overgrown bubble/rear reaches its maximum, Figs. 11-14c, and starts to collapse towards the molten droplet. The accelerating interface hits the molten droplet, adding the coolant into the interaction zone. At this point (t=0 ms), the actual direct melt-coolant contact/mixing takes place, Figs. 11-14d, which leads to the bubble's second cycle characterized by the explosive evaporation and fine fragmentation of the melt droplet. The produced fine fragments set off in the radial direction following the interface of the growing bubble, forming a shell-like region of finely fragmented melt particles. As the vapor bubble decelerates, the inertia continues to drive the fine fragments to penetrate deeper into the liquid domain. The bubble reaches its maximum size, Figs. 11-14e, and subsequently collapses, leaving the fine fragments behind whereas a fraction of them is redistributed in the center region of the original droplet. At this point in time, the bubble dynamics cannot be precisely discerned since the cloud of fine fragments unable the exact resolution of the vapor interface. Nevertheless, the bubble's third cycle can still be recognized, when the collapsing bubble promotes the mixing of the coolant and the remains of the molten material, Figs. 11-14f, leading to a secondary explosive vaporization, Figs. 11-14g. The fine fragments are then dispersed within the coolant after the bubble has finally collapsed.

No apparent dissimilarities in the vapor film and melt dynamics were found for the test series under high melt superheat (Figs. 11 and 12): both melt compositions, i.e. eutectic and non-eutectic WO_3-CaO, consistently led to explosive vapor generation and subsequent fine fragmentation of the droplet in three cycles. Conversely, the test series with non-eutectic WO_3-CaO under lower melt superheat (Fig. 14) reveal the presence of portions of a crust on the second cycle during fragmentation, Fig 14e-f, while the eutectic tests (Fig. 13) regularly led to the fine fragmentation of melt droplet similar to the high superheat tests.

Differences in melt fragmentation will directly influence the vapor explosion energetics, since it is an indication of the amount of melt involved in the interaction, besides defining the heat transfer area. Accordingly, one should expect a milder interaction in the low superheat non-eutectic experiments, given that the fine fragmentation is diminutive.

The equivalent diameter, normalized by its value prior to the external disturbance, is shown in Figure 15 for eutectic (e) and non-eutectic (ne) mixtures of WO_3-CaO and different melt superheat. One can clearly identify the three cycles mentioned previously. In the high melt superheat tests, both melt compositions cover a wide spectrum of the vapor film history and no particularity can be discerned, Fig. 15a. The lower melt superheat tests, Fig. 15b, appear to show a tendency of a more pronounced the 2nd and 3rd cycles in the non-eutectic runs; however a clearer picture of such differences should arise by evaluating the energetics associated with the interaction.

From the bubble radial history, one can estimate the work done by the expanding bubble and thus the steam explosion conversion ratio. One should keep in mind that it is not viable to estimate the conversion ratio up to the third cycle due to the fragments dispersed in the coolant, which disables the accurate resolution of the vapor film interface. For this reason, the following analysis will be based on the energetics up to the second cycle, given that the correlation with the melt preconditioning, prerequisite for an energetic vapor explosion in

thermal fragmentation regime, will be conserved, i.e. high melt preconditioning would lead to a higher second cycle conversion ratio [18].

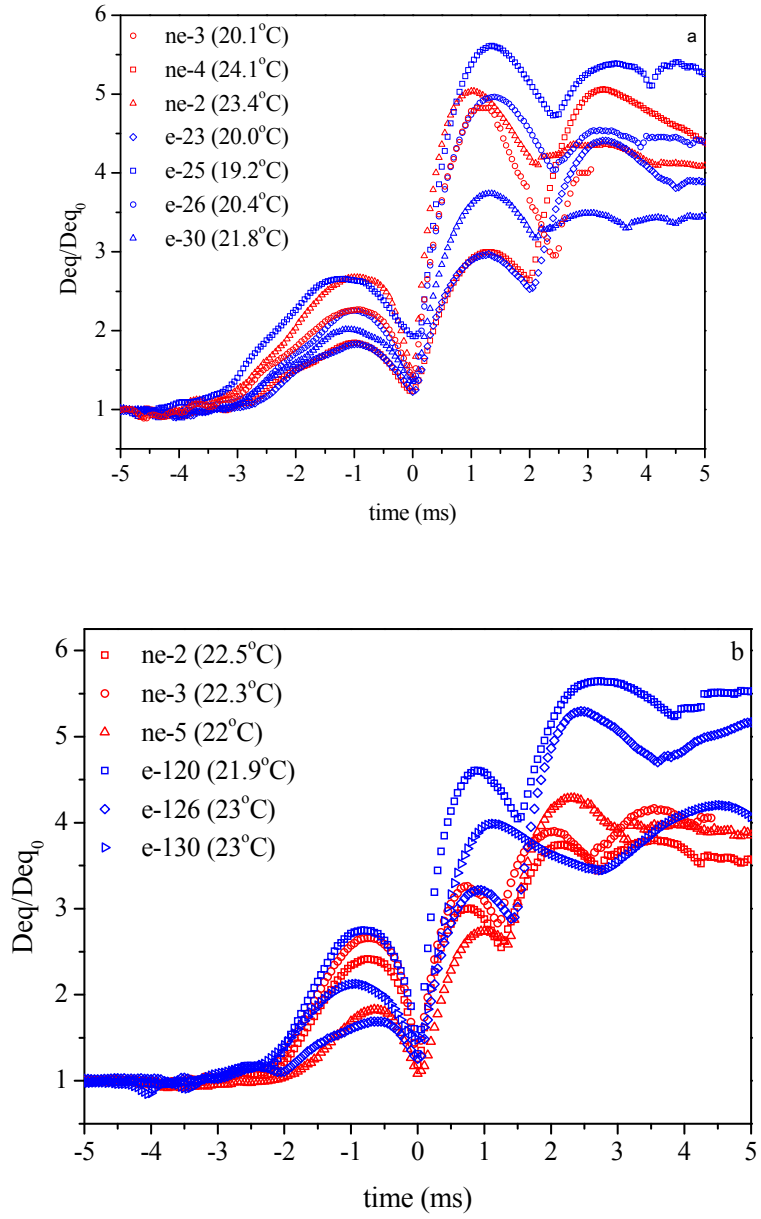

Fig. 15: Radial history of eutectic (e) and non-eutectic (ne) WO_3-CaO single droplet for high (a) and low (b) melt superheat, with the respective water temperature.

The melt preconditioning, i.e. deformation/pre-fragmentation of a molten droplet during the first bubble cycle, is quantified by the droplet's projected area evolution depicted in the radiographic images.

Figure 16a points out to no apparent differences between the eutectic and non-eutectic tests with high melt superheat in terms of steam explosion energetics and preconditioning, which is a reflection of what is seen in the bubble dynamics, Fig. 15a. In contrast, Figure 16b

shows a divergence between the energetics and melt preconditioning of the eutectic and non-eutectic tests, i.e. non-eutectic test led to a milder interaction than the eutectic tests.

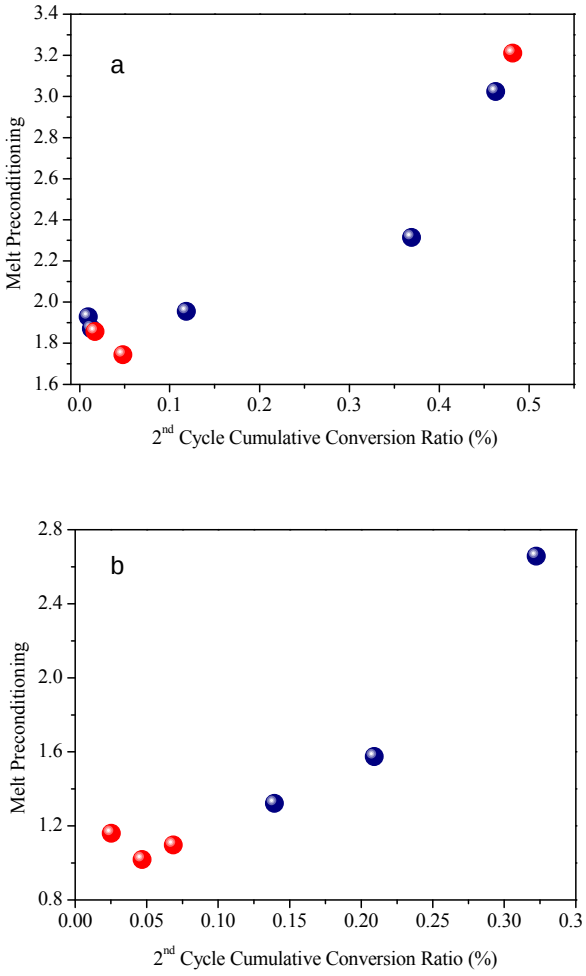

Fig. 16: Melt droplet preconditioning and 2nd cycle cumulative conversion ratio of eutectic (blue) and non-eutectic (red) WO_3-CaO single droplet for high (a) and low (b) melt superheat.

Such observations can be rationalized by considering the phase change of a non-eutectic binary oxidic melt droplet, e.g. solidification and/or formation of a mushy phase, that typically occurs over a specific temperature range determined by the liquidus and solidus line. Accordingly, if the droplet superheat is high enough the material phase will be kept far above the liquidus line, i.e. in liquid form, during the interaction for both melt compositions. That is to say, that the melt droplet will be away from the region in which solidification behaviors would play a role on the melt preconditioning and thus in the steam explosion energetics, Fig. 16a.

Then again, in the case of low superheat experiments, the melt temperature falls into such specific temperature range, i.e. between the liquidus and solidus line for the non-eutectic material, which can be augmented by the difference in undercooling characteristic of such fast quenching (direct melt-coolant contact) [20]. In fact, for non-eutectic materials, it

suffices to remove only a fraction of the latent heat of fusion to bring the melt into a mushy state.

Once in this regime, formation of a thin crust or even a mushy layer on the droplet's surface would significantly increase the viscosity and effective surface tension, rendering the droplet resilience to external forcing, including external disturbances due to local melt-coolant contacts [19]. Correspondingly, the non-eutectic WO_3-CaO melt droplet shows a diminutive melt preconditioning due to such deformation resistant state, which then reflects on the vapor explosion conversion ratio, Fig 7b. Moreover, the consistent presence of a crust, Fig 5e-g, on the non-eutectic tests implies less melt material available for the interaction, contributing to the differences in energetics between eutectic and non-eutectic tests.

In summary, the estimated energetics points out to a milder interaction for the non-eutectic melt composition in the low superheat tests, particularly when compared to the tests with the melt droplet in a eutectic composition. Moreover, a thin crust was observed in the non-eutectic during the explosive 2nd cycle. Such differences could not be perceived in the tests with high melt superheat, which consistently led to the fine fragmentation of the melt droplet. The MISTEE data on the melt preconditioning (melt droplet deformation/pre-fragmentation established during the bubble's 1st cycle) confirm its direct relation to the interaction's conversion ratio, and implicate the governing role of the melt material on the triggering of a single binary oxide droplet vapor explosion. Namely, the distinction between eutectic and non-eutectic WO3-CaO in the actual tests lies on the solidification characteristics of the melt droplet during the direct melt-coolant contact. However, for the same initial melt superheat, the material effect of a binary oxide on the vapor explosion energetics can only be perceived when the melt droplet is in a quite specific temperature range, raising a question of its actuality on a large scale vapor explosion.

3. Concluded Remarks

Significant progress was made and important findings were obtained in the INCOSE project during year 2010. Substantial advances in process modeling and new insights into related phenomena and mechanisms were gained from the studies on i) debris bed coolability with focus on characterization of the effective particle diameter of irregular particles as found in debris beds; i) molten corium coolability in the BWR lower head and vessel creep failure by coupled assessment for taking into account the CRGT cooling as a potential SAM measure; and iii) micro dynamics of a single droplet steam explosion by using binary oxidic simulant (WO_3-CaO) of corium.

Specifically, for a particulate bed packed with non-spherical particles, the effective particle diameter can be represented by the equivalent diameter of the particles, which is the product of Sauter mean diameter and shape factor of the particles. Method for one-way coupling of PECM model with ANSYS solid mechanical simulation was developed to analyze creep failure of the lower head under melt pool attack with CRGT cooling. The results revealed two different modes of vessel failure: a 'ballooning' of the vessel bottom and a 'localized creep' concentrated within the vicinity of the top surface of the melt pool. The steam explosion experiments using oxidic mixture of WO3-CaO at low superheat (100 ^{o}C) show that there is a difference in steam explosion energetics between the eutectic and no-eutectic materials. Notably, one PhD thesis [18] related to steam explosion exegetics was defended

in November 2010. More achievements and detailed descriptions can be found in the related publications [14-22]. Overall, the research of INCOSE Project has advanced the knowledge of steam explosion and in-vessel coolability toward reducing conservatism in quantification of corium melt risks in BWRs.

References

[1] V.K. Dhir, Boiling and two-phase flow in porous media, *Annual Review of Heat Transfer*, **5**: 303-350, CRC Press, Boca Raton, 1994.

[2] R.J. Lipinski, A one dimensional particle bed dryout model. ANS Transactions, **38**: 386-387, 1981.

[3] R.J. Lipinski, "A coolability model for post accident nuclear reactor debris", *Nulcear Technology*, **65**: 53-66 (1984).

[4] A.W. Reed, The effect of channeling on the dryout of heated particulate beds immersed in a liquid pool. PhD thesis, Massachusetts Institute of Technology, Cambridge, 1982.

[5] K. Hu and T.G. Theofanous, On the measurement and mechanism of dryout in volumetrically heated coarse particle beds, *Int. J. Multiphase Flow*, **17** (4): 519-532, 1991.

[6] T. Schulenberg and U. Műller, An improved model for two-phase flow through beds of course particles, *Int. J. Multiphase flow*, **13** (1): 87-97, 1987.

[7] S. Ergun, Fluid flow through packed columns, *Chemical Engineering Progress*, **48** (2): 89-94, 1952.

[8] S. L. Soo, Multiphase Fluid Dynamics, New York: Science press Gower Technical, 1990.

[9] L.X. Li, W.M. Ma, Experimental characterization of effective particle diameter of a packed bed with multi-diameter spheres, *Nuclear Engineering and Design*, **241** (5): 1736-1745, 2011.

[10] P.C. Carman, Fluid flow through packed beds. *Trans. Inst. Chem. Eng*. **15**: 150-166, 1937.

[11] E.A. Foumeny, F. Benyahia, J.A. Castro et al., Correlations of pressure drop in packed beds taking into account the effect of confining wall. *Int. J. Heat Mass Transf*. **36** (2): 536-540, 1993.

[12] D. Nemec and J. Levec, Flow through packed bed reactors: 1. Single-phase flow. *Chem. Eng. Sci*. **60**: 6947-6957, 2005.

[13] H. Wadell, Volume, Shape and Roundness of Quartz Particles. *J. Geol*. **43**: 250-280, 1935.

[14] L.X. Li and W.M. Ma, Experimental study on the effective particle diameter of a packed bed with non-spherical particles, *Transport in Porous Media*, in press.

[15] C.T. Tran and P. Kudinov, A synergistic use of CFD, experiments and Effective Eonvectivity Model to reduce uncertainty in BWR severe accident analysis, CFD4NRS-3 Workshop, Bethesda, MD, USA, September 14-16, 2010.

[16] W. Villanueva, C.T. Tran and P. Kudinov, Coupled thermo-mechanical creep analysis for boiling water reactor pressure vessel lower head, The 8th International Topical Meeting on Nuclear Thermal-Hydraulics, Operation and Safety (NUTHOS-8), Shanghai, China, October 10-14, 2010.

[17] R. C. Hansson, T. N. Dinh and H. S. Park, Simultaneous High Speed Digital Cinematographic and X-ray Radiographic Imaging of an Intense Multi-Fluid Interaction with Rapid Phase Changes, *Experimental Thermal and Fluid Sciences*, **33**: 754-756, 2009.

[18] R. C. Hansson, An experimental study on the dynamics of a single droplet vapor explosion, PhD Thesis, Royal Institute of Technology, Stockholm, 2010.
[19] R.C. Hansson, H.S. Park, T.N. Dinh, Dynamics and preconditioning in a single droplet vapor explosion, *Nuclear Technology*, **167**: 223-234, 2009.
[20] T. N. Dinh, Material property effect in steam explosion energetics: revisited, NURETH-12, Pennsylvania, USA, September 30-October 4, 2007.
[21] *Proc. of the 30th Review Meeting for Project "Melt-Structure-Water Interactions in a Severe Accident"* (MSWI-30), KTH, Stockholm, Sweden, June 10, 2010, 105p.
[22] *Proc. of the 31st Review Meeting for Project "Melt-Structure-Water Interactions in a Severe Accident"* (MSWI-31), KTH, Stockholm, Sweden, December 9, 2010, 90p.

Title	In-vessel Coolability and Steam Explosion in Nordic BWRs
Author(s)	Weimin Ma, Liangxing Li, Roberta Hansson, Walter Villanueva, Pavel Kudinov, Louis Manickam, Chi-Thanh Tran
Affiliation(s)	Royal Institute of Technology (KTH), Sweden
ISBN	978-87-7893-318-8
Date	May 2011
Project	NKS-R / INCOSE
No. of pages	23
No. of tables	4
No. of illustrations	16
No. of references	22

Abstract

The objective of this research is to reduce the uncertainty in quantification of steam explosion risk and in-vessel coolability in the Nordic BWR plants which employ cavity flooding as severe accident management (SAM) strategy.

To quantify the coolability of debris bed packed with irregular particles, the friction laws of fluid flow in particulate beds packed with non-spherical particles were investigated on the POMECO-FL test facility, and the experimental data suggest that the Ergun equation is applicable if the effective particle diameter of the particles is represented by the equivalent diameter of the particles, which is the product of Sauter mean diameter and shape factor of the particles. One-way coupling analysis between PECM model for melt pool heat transfer and ANSYS thermo-structural mechanics was performed to analyze the vessel creep, and the results revealed two different modes of vessel failure: a 'ballooning' of the vessel bottom and a 'localized creep' concentrated within the vicinity of the top surface of the melt pool. Single-droplet steam explosion experiments were carried out by using oxidic mixture of WO_3-CaO, and the results show an apparent difference in steam explosion energetics between the eutectic and non-eutectic melts at low melt superheat (100 ^oC).

Key words severe accident, debris coolability, steam explosion

Available on request from the NKS Secretariat, P.O.Box 49, DK-4000 Roskilde, Denmark.
Phone (+45) 4677 4045, fax (+45) 4677 4046, e-mail nks@nks.org, www.nks.org